Quantitative spectroscopic characterization of near-UV/visible E. coli (pYAC4), B. subtilis (PY79), and green bread mold fungus fluorescence for diagnostic applications

Highlights

Quantitative spectroscopic characterization of near-UV/visible *E. coli* (pYAC4), *B. subtilis* (PY79), and green bread mold fungus fluorescence for diagnostic applications

Joshua M. Herzog,Volker Sick

- UV-visible fluorescence is a promising method to detect and identify microbe species
- Fluorescence spectra and intensity are similar between *E. coli*, *B. subtilis*, and green bread mold fungus
- Microbial fluorescence of selected species is likely due to NADH and FAD
- Performance analysis suggests that as few as 35 *E. coli* cells can be detected using UV-fluorescence

Quantitative spectroscopic characterization of near-UV/visible *E. coli* (pYAC4), *B. subtilis* (PY79), and green bread mold fungus fluorescence for diagnostic applications

Joshua M. Herzog[a,*], Volker Sick[a]

[a]Department of Mechanical Engineering, University of Michigan, 2350 Hayward St., Ann Arbor, MI 48109, USA

ARTICLE INFO

Keywords:
fluorescence
microbe
imaging diagnostics
E. coli
B. subtilis

ABSTRACT

Ultraviolet (UV)-excited visible fluorescence is an attractive option for low-cost, low-complexity, rapid imaging of bacterial and fungal samples for imaging diagnostics in the biomedical community. While several studies have shown there is potential for identification of microbial samples, very little quantitative information is available in the literature for the purposes of diagnostic design. In this work, two non-pathogenic bacteria samples (*E. coli* pYAC4, and *B. subtilis* PY79) and a wild-cultivated green bread mold fungus sample are characterized spectroscopically for the purpose of diagnostic design. For each sample, fluorescence spectra excited with low-power near-UV continuous wave (CW) sources, and extinction and elastic scattering spectra are captured and compared. Absolute fluorescence intensity per cell excited at 340 nm is estimated from imaging measurements of aqueous samples. The results are used to estimate detection limits for a prototypical imaging experiment. It was found that fluorescence imaging is feasible for as few as 35 bacteria cells (or ∼30 μm^3 of bacteria) per pixel, and that the fluorescence intensity per unit volume is similar for the three samples tested here. A discussion and model of the mechanism of bacterial fluorescence in *E. coli* is provided.

1. Introduction

Low-cost, accurate, and rapid screening of pathogens are needed in a variety of point-of-care and industrial settings. There are, for example, 600 million annual cases of food-borne illness and over 400,000 deaths worldwide caused by contaminated food supplies [1]. Similarly, healthcare associated infections, or infections that patients acquire while receiving healthcare, affect almost 2 million hospitalized patients per year in the United States (US) and more than 5% of these patients die as a result [2]. Likewise, the problem of wound and wound-associated infections is growing sharply in the US, with estimated Medicare costs for treatment between $28 and $96 billion in 2014 [3].

Improved diagnostic tools for bacterial and fungal infections provide a means to help reduce this burden through improved detection and identification of contamination and infection. Near-ultraviolet (UV) induced fluorescence is an attractive imaging tool because it is generally low-cost, rapid, and amenable to automation. UV-induced fluorescence has relatively recently been shown to be capable of identification of bacteria down to the family, genus, species, and subspecies levels [4]. Intrinsic microbial fluorescence is largely the result of aromatic amino acids (typically excited at deeper UV wavelengths), and co-enzymes including nicotinamide adenine dinucleotide (NADH) and flavin adenine dinucleotide (FAD) excited at near-UV and optical wavelengths. Several studies have characterized UV-induced fluorescence in bacteria [5, 6, 7, 8] and found that spectra are similar, but were successful in distinguishing between samples using techniques including principal component analysis (PCA). Several studies have also considered UV-induced fluorescence of fungi samples [9, 10, 11] and observed similar spectra and noted similar performance for detection and classification of samples primarily using PCA.

Earlier work focused primarily on using spectral decomposition methods to distinguish between a limited set of bacteria or fungi and as a result there is much information missing in the literature that is needed for diagnostic design calculations. Precise measurements or models of fluorescence spectra for a variety of species, and especially those that are implicated in human health, are lacking. Although it is known that fluorescence properties depend on the metabolic state of the microbe [4] due to changes in chemical composition, we do not have a quantitative understanding of the impact on fluorescence properties. It has also been acknowledged that there is a widespread lack of quantitative reporting and analysis in bacterial fluorescence studies [12] resulting in significant biases, which suggests that much of the existing bacterial fluorescence data may not be sufficiently accurate for diagnostic design.

As a first step towards developing low-cost fluorescence-based imaging tools for detection and discrimination of microbial species, an initial characterization of two bacteria samples, *E. coli* (pYAC4), *B. subtilis* (PY79), and a wild-type green bread mold fungus was performed using low-cost optical components and low-power light-emitting diode (LED) sources using a line-of-sight configuration which is believed to be representative of potential low-cost imaging solutions. This manuscript reports on an initial detailed radiometric characterization of individual samples from several species to provide data needed for the design of novel fluorescence imaging tools; interference from body fluids

*Corresponding author
jmherzog@umich.edu (J.M. Herzog)
ORCID(s): 0000-0001-9089-819X (J.M. Herzog); 0000-0001-5756-9714 (V. Sick)

or tissues, the impact of metabolic state on microbial fluorescence, and sample-to-sample variability are outside the scope of this work but will be considered in future studies.

2. Methods & Materials

Two non-infectious bacteria species, *E. coli* (pYAC4) and *B. subtilis* (PY79), and a wild-cultivated green bread mold fungus were characterized spectroscopically. Fluorescence, extinction, and elastic scattering spectra were measured from microbial smears, and fluorescence intensity was measured from aqueous suspensions. The preparation of samples, data collection, and data analysis procedures are described in the following sections.

2.1. Microbial samples

B. subtilis (PY79) and *E. coli* (pYAC4) samples were received on nutrient agar plates. pYAC4 cultures were stored at 4°C and removed to room temperature approximately 30 minutes prior to performing experiments. PY79 cultures were maintained at room temperature and used within 24 hours of incubation. Green bread mold samples were cultivated at room temperature from spoiled bread.

Microbial smears were prepared on 3 mm thick fused silica windows. Sterile inoculation loops were used to collect 1-3 mm^3 of culture per sample. The collected culture was spread over a small circular region, ∼1 cm in diameter, in the center of the fused silica substrate. Aqueous solutions were prepared in a similar fashion; sterile inoculation loops were used to collect 1-3 mm^3 of culture per sample. The loop ends were placed in a clean, 20 mm × 30 mm × 40 mm UV-grade fused silica cuvette (Lambda Physik 40 mm cuvette, FL 464) and rinsed with distilled water. The cuvette was then filled to a height of approximately 25 mm and stirred vigorously until the culture was well-mixed.

A Helium-Neon (HeNe) laser (Melles Griot 05-LLR-811) module was used to determine cell density in the aqueous suspension via elastic scattering. A low-noise scientific complementary metal-oxide semiconductor (CMOS) camera (LaVision Imager sCMOS) was used to image elastic scattering at normal incidence. A flatfield correction was performed using an LED screen. The scattering intensity along the centerline of the beam was used to estimate cell density via the Beer-Lambert law,

$$\frac{I}{I_0} = \exp\left(-n\sigma_s z\right) \tag{1}$$

where I is the measured intensity at axial location z, n is the cell density, and σ_s is the scattering cross-section evaluated at the HeNe laser wavelength of 632.8 nm. The centerline of the beam is taken to avoid the bias from forward-scattered light. The object-plane pixel size of 10 μm is believed to be sufficiently small that single-scattering is dominant within this region. The scattering cross-section for pYAC4 is calculated from Mie scattering theory using the volume-equivalent cell radius of 0.6 μm for an average volume of 0.9 μm^3 using parameters from [13] resulting in a cross-section of 0.2 μm^2; this method is believed to be robust because the Mie scattering solution is insensitive to scattering parameter at such low relative refractive indices. The scattering cross-section for *B. subtilis* is taken as the extinction coefficient measured at 632.8 nm from [14] and is 1 μm^2.

For the green bread mold fungus elastic scattering from individual particles was observed which enabled direct measurement of number density via particle counting, and the extinction coefficient was measured via an ensemble average over 200 scattering images. The scattering cross-section was calculated from the extinction coefficient and number density measurement, and a particle size was estimated from the scattering cross-section.

The particle counting algorithm is as follows. A threshold is applied to identify regions that contain particle image patterns. Morphological operations (dilation and erosion with 1 pixel radii) are applied to the mask to remove artifacts. A distance transform is calculated from the mask, and a watershed transformation is applied which segregates the image into regions belonging to a single particle. The particle location is then determined from the centroid of the image intensity within each watershed region. Additional properties such as particle image size and intensity are also calculated from each region.

2.2. Fluorescence spectra

Fluorescence spectra for each microbial smear sample was measured using a 127 mm focal length spectrometer (Newport Oriel MS127i, Model 77480) with a thermoelectrically cooled scientific charge-coupled device (CCD) camera (LaVision ImageIntense). Fluorescence emission was captured using a fiber-coupled lens (ThorLabs F810SMA-635) focused onto the end of a fiber bundle that was fed into the entrance slit of the spectrometer. The camera was exposed for 1 second, hardware binned 16x1, and software binned to cover the height of the entrance slit. The spectral resolution is estimated to be ∼3 nm based on the full width at half maximum (FWHM) of the Hg-spectrum G-line at 435.8 nm. Samples were excited at 340 nm (ThorLabs M340L4) and 370 nm (Thorlabs LED370E) using fixed-wavelength LED modules. Several additional measurements were made of *E. coli* only using 390, 405, and 455 nm low-power LED modules for comparison. Measurements with the low-powered stock LEDs additionally made use of an image intensifier (LaVision Intensified Relay Optics) for increased sensitivity. The intensifier was gated for 100 ms when used. A combination of band-pass and long-pass filters were used to restrict the excitation band, and to avoid capturing scattered or reflected excitation light, respectively. The filter and LED specifications for each excitation band are given in Table 1, and the LED emission spectrum and band-pass filter transmission spectra for the primary 340 and 370 nm excitation schemes are plotted in Figure 1. To maximize collection and excitation efficiency, the optics were aligned axially (*i.e.*, the excitation source and collection lens were

Table 1
Filters and LED modules used for fluorescence spectra measurements. Radiant power (Φ) and divergence (α) are manufacturer-provided specifications; irradiance (I) is estimated based on the approximate sample location, LED manufacturer specifications, and bandpass filter transmission. Optical power and divergence figures are not available for the DiCuno LEDs; the electrical power dissipated by these LEDs is approximately 60 mW.

Band	LED	BP filter	LP filter	Φ [mW]	α [°]	I [$\frac{mW}{cm^2}$]
340 nm	ThorLabs M340L4	ThorLabs FB340-10	ThorLabs FELH0400	60	110	5
370 nm	ThorLabs LED370E	ThorLabs FB370-10	ThorLabs FELH0400	2.5	19	5
390 nm	DiCuno 5 mm UV LED	Andover 390FS10-50	Edmund Optics #84-742	-	-	-
405 nm	Thorlabs LED405E	Andover 400FS40-50	Edmund Optics #84-742	10	5	10
455 nm	DiCuno 5 mm blue LED	Andover 456FS10-50	Edmund Optics #64-635	-	-	-

on opposite sides of the sample). A schematic of the experimental setup is shown in Figure 2. LED excitation was continuous wave (CW). Spectra were corrected for background and for relative spectral response using a quartz-tungsten halogen (QTH) lamp (World Precision Instruments, D2H), and were averaged over 100 to 500 exposures, depending on recorded intensity. Background measurements were taken with the LED off and sample in place to ensure any ambient background light is subtracted correctly; measurements of the clean substrate exhibited negligible fluorescence.

2.3. Extinction and elastic scattering spectra

Extinction spectra were recorded for each smear using a similar experimental setup as described in Section 2.2, with the LED source replaced by a deuterium arc lamp and quartz-tungsten halogen lamp combination (World Precision Instruments, D2H) and band-pass filters removed. All measurements used the combined deuterium arc lamp and quartz tungsten halogen outputs. The *E. coli* extinction measurements additionally made use of the image intensifier to investigate deeper UV extinction. Measurements were averaged over 500 to 1000 exposures. The LED source and sample were then rotated (see inset diagram in Figure 2) to measure elastic scattering spectra of *E. coli*. The extinction spectrum is calculated as

$$k_e L = -\log \frac{I_t - B}{I_0 - B} \tag{2}$$

where k_e is the extinction coefficient, I_t is the transmitted intensity, I_0 is the source or incident intensity, B is the background intensity, and L is the sample thickness. Note that this analysis ignores the contribution of surface reflections from the glass window for simplicity. The Fresnel reflection coefficient for fused silica in air is approximately 3-4% per surface assuming a refractive index of 1.46 and is small compared to the microbial extinction. The scattering coefficient is calculated here as

$$k_s = \frac{I_s - B}{I_0 - B} \tag{3}$$

where I_s is the scattered light intensity. Since this expression does not account for differences in collection efficiency, exposure, and sample thickness, the units of k_s reported here are arbitrary.

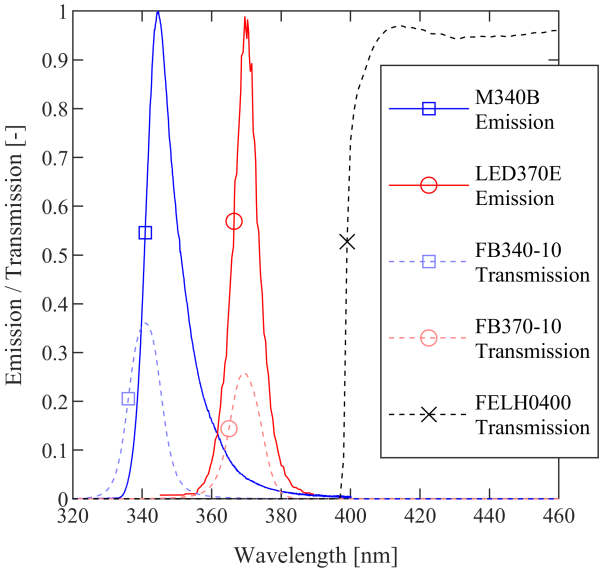

Figure 1: Emission bands of the two LED excitation sources with band-pass filter transmission spectra superimposed.

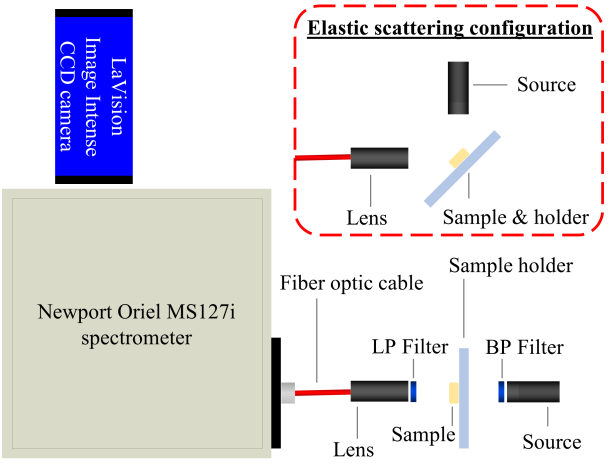

Figure 2: Experimental setup diagram for spectroscopy measurements. The dashed box indicates the altered source and sample configuration used for elastic scattering measurements.

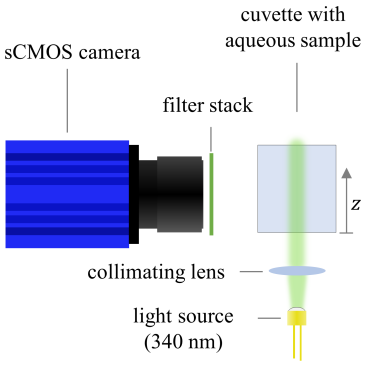

Figure 3: Experimental setup diagram for absolute intensity characterization experiments.

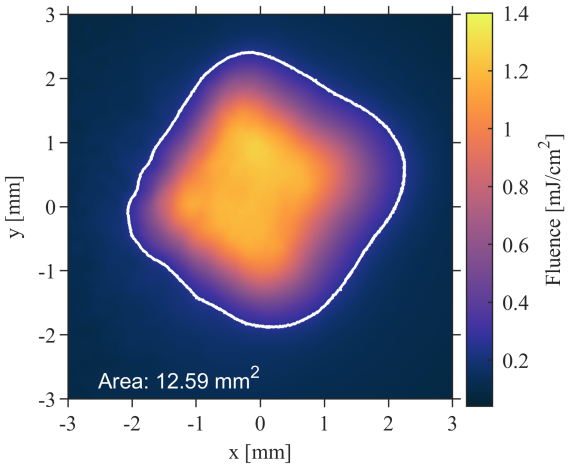

Figure 4: LED fluence profile measured in the object plane measured by fluorescence of a paper target at 45° angle of incidence. Fluence is calculated for a 100 ms exposure duration. The white outline indicates the extent of the source based on a threshold calculated with Otsu's method [15].

2.4. Absolute fluorescence intensity

Absolute intensity measurements were performed using the 340 nm LED module (ThorLabs M340B with LEDD1B driver) with the LaVision Imager sCMOS camera on the aqueous samples. Figure 3 shows the experimental setup used for the measurements.

The LED module was outfitted with the 340 nm bandpass filter (ThorLabs FB340-10) resulting in ∼16% transmission. The LED output was collimated using a 30 mm diameter, 25 mm focal length spherical UV-grade fused silica lens and directed into the cuvette. The source fluence profile was measured using the luminescence from a paper sample angled at 45 degrees relative to the object plane and is plotted in Figure 4. From the plot, the width of the source along the centerline is approximately 3.5 mm. The peak source irradiance was measured using a photodiode (ThorLabs DET10A) and voltmeter (Fluke 117) and found to be 13 mW/cm^2 (corresponding to 1.3 mJ/cm^2 peak fluence for a 100 ms exposure); this value is consistent with the estimated 20% collection efficiency of the collimating lens.

HeNe scattering and luminescence images were taken with an exposure duration of 100 ms using a Nikon Nikkor $f/1.4$, 50-mm lens. A 2 mm Schott GG-420 filter was placed in front of the lens to block scattered UV light. Both scattering and luminescence images were background subtracted and flatfield corrected using an image of an LED screen placed in the object plane; flatfield corrections were on the order of at most 20% of the average image intensity. A series of 100-200 images were taken for each experiment and averaged to reduce noise. Background images were taken with the sample in place and LED off to ensure ambient light is subtracted correctly.

Fluorescence intensity per cell is calculated from the peak measured signal intensity on the image sensor. The measured intensity in counts is related to the isotropic fluorescence intensity in photons per cell via

$$S = N_{p/c} n V_o \frac{\Omega}{4\pi} \frac{\eta_{opt}\eta_{QE}}{C_{A/D}} \eta_{ext} = G n V_o N_{p/c} \tag{4}$$

where $N_{p/c}$ is the number of photons emitted per cell, n is the cell number density, and V_o is the collection volume in the object plane. The quantity Ω is the collection solid-angle, η_{opt} and η_{QE} are the optical and quantum efficiencies of the optical elements and detector, and $C_{A/D}$ is the analog-to-digital conversion gain of the sensor. The parameter η_{ext} represents the fraction of light that is not scattered as it exits the cuvette. On the right-hand side, the system gain factor G is calculated and includes all of the efficiency factors. The parameters were estimated from manufacturer specifications and theory, and are listed in Table 2. Estimated relative uncertainty in each radiometric quantity is included in the table; the total radiometric uncertainty is approximately 50% and is dominated by uncertainty in the effective quantum efficiency and attenuation.

Assuming a linear response, the fluorescence intensity per cell is related to the incident fluence by

$$N_{p/c} = \sigma_c \phi \frac{E''}{\hbar\omega} \tag{5}$$

where σ_c is the total absorption cross-section of the cell, ϕ is an effective fluorescence quantum yield (FQY) for the cell, $\hbar$ is the reduced Planck constant, ω is the angular frequency of the excitation source, and E'' is the LED source fluence. A fluorescence coefficient can also be defined as

$$k_f = \frac{N_{p/c}}{V_c \frac{E''}{\hbar\omega}} = \frac{\sigma_c \phi}{V_c} \tag{6}$$

where V_c is the average cell volume; defined this way, the fluorescence coefficient provides a measure of fluorescence intensity per unit volume and is convenient for comparison. The uncertainty in k_f is approximately 50% and is dominated by radiometric uncertainties listed in Table 2. There are additional contributions from uncertainty in cell concentration, cell volume, and excitation source fluence; however, these contributions are expected to be small compared to the radiometric uncertainty.

Table 2
Geometric and optical parameters for the experimental setup. Quantum efficiency includes the Schott GG-420 filter.

Symbol	Description	Value			Units	Uncertainty
		E. coli	*B. subtilis*	Mold		%
$f_{\#}$	lens f-number	1.4	4	1.4	-	0
l_{px}	object-plane pixel size	10	10	10	μm	5
M	magnification	-0.65	-0.65	-0.65	-	5
$\frac{\Omega}{4\pi}$	collection fraction	0.005	6.3×10^{-4}	0.005	-	6
η_{opt}	optical efficiency	0.9	0.9	0.9	-	10
η_{ext}	attenuation	0.5	0.5	1	-	30
η_{QE}	quantum efficiency	0.35	0.35	0.35	e^-/γ	20
$C_{A/D}$	ADU gain	2.2	2.2	2.2	e^-/ADU	5
L	collection volume depth	3	3	3	mm	20
G	System gain	1.7×10^{-3}	2.1×10^{-4}	3.4×10^{-3}	ADU/γ	50

2.5. Fluorescence imaging

Fluorescence imaging was performed for *E. coli* smears at 370, 390, and 455 nm using the sources and filters in Table 1. Images were acquired with the LaVision Imager sCMOS camera with a 50-mm, $f/1.4$ lens (Nikon AF Nikkor 50mm f/1.4D), and exposures of 10 ms. A series of 100 fluorescence images were taken at 10 Hz and averaged to reduce noise. Images were background subtracted and flatfield corrected using the measured LED profile.

3. Results

Fluorescence spectra for each sample excited at 340 and 370 nm were measured, along with extinction and elastic scattering spectra at near UV and optical wavelengths. Absolute fluorescence intensity measurements were also made for each species using 340 nm excitation. For *E. coli*, fluorescence spectra excited at 390, 405, and 455 nm were collected for comparison. Finally, a series of fluorescence images were taken to demonstrate the capability of fluorescence imaging using low-power LED excitation at near UV and optical wavelengths with exposure durations that are suitable for video-rate imaging.

3.1. Fluorescence spectra

Fluorescence spectra for each sample at 340 and 370 nm excitation are shown in Figure 5, normalized by their integral over the measurement range (405-535 nm). From the plot, two distinct peaks appear in each sample; one near approximately 440-450 nm, and another near 530 nm. There additionally appears to be a third peak near 410-420 nm, particularly in the mold sample at 370 nm excitation. Peaks in *E. coli* near 450 and 530 nm have been observed and largely attributed to NADH [5, 16] and flavins such as FAD [17], respectively.

Interestingly, there are noticeable differences between species particularly at 370 nm excitation; the mold species has the strongest peak near 440 nm and an additional peak near 410-420 nm, while *B. subtilis* peaks near 450 and exhibits a much brighter long-wavelength tail. *E. coli* lies somewhere between these two throughout the range. It is additionally interesting to note that increasing the excitation wavelength from 340 to 370 nm results in a reduction in the relative magnitude of the 440 nm peak, which is consistent with the reduced absorption cross-section of NADH at 370 nm compared to 340 nm [18].

A series of *E. coli* fluorescence spectra excited at 340, 370, 390, 405, and 455 nm are shown in Figure 6. The spectra were scaled to have the same fluorescence intensity in overlapping regions between adjacent excitation wavelengths (*e.g.*, the 340 and 370 nm spectra are scaled to the same intensity where they overlap between 500 and 550 nm). As excitation wavelength is increased from 340 to 405 nm, significant reduction in blue fluorescence ($\lesssim$500 nm) is observed relative to green fluorescence. This is consistent with reduced absorption by NADH as expected from [18] for a fixed FQY. The shape of the 530 nm fluorescence band does not appear to change significantly with excitation wavelength, and this behavior is consistent with measured FAD absorption spectra from 340 to 455 nm that show broad, slowly-varying features [19].

3.2. Absolute fluorescence intensity

The measured fluorescence intensity along the centerline of the images for each sample is shown in Figure 7. The measured extinction coefficients k_e, estimated cell number density n_c, effective volume-equivalent diameter $\langle d_c \rangle$, peak fluorescence intensity S, emitted photons per cell $N_{p/c}$, emitted photons per unit volume N_V, and fluorescence coefficient k_f are listed in Table 3. From the table, large variation in fluorescence intensity per cell was observed with the mold sample having the strongest fluorescence. Normalizing the fluorescence intensity by the assumed cell volume results in a value that is nearly constant within the estimated uncertainty (50%) between the samples. However, this data is sufficient to provide an order of magnitude estimate for predicting diagnostic or imaging performance, and is sufficient to show that fluorescence intensities are similar between the selected species on a volumetric basis.

Mold spore diameter was estimated from a second suspension with measured extinction coefficient of 0.036 mm^{-1} with number density approximately 100 mm^{-3} based on the

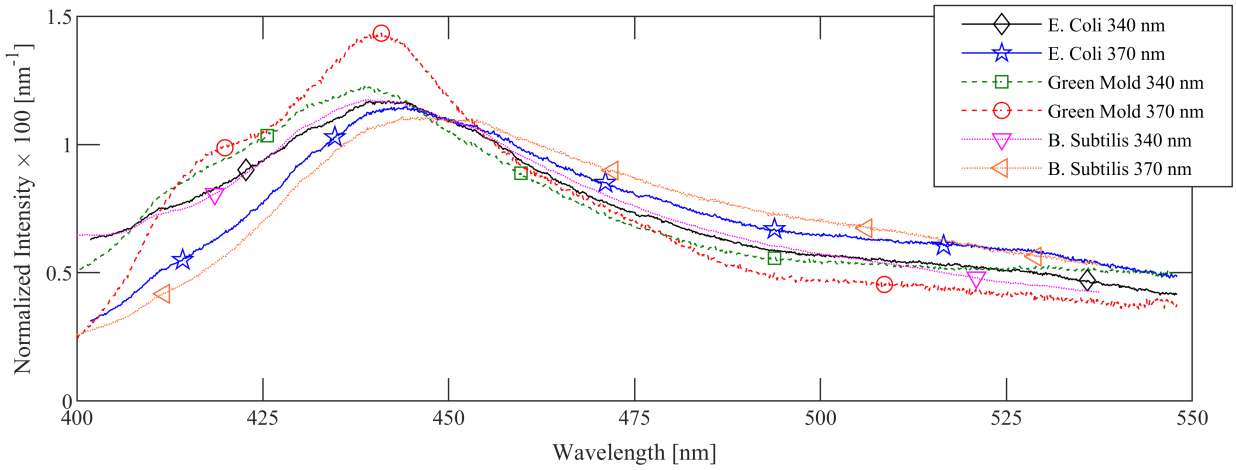

Figure 5: Measured fluorescence spectra for microbial smears at 340 and 370 nm LED excitation.

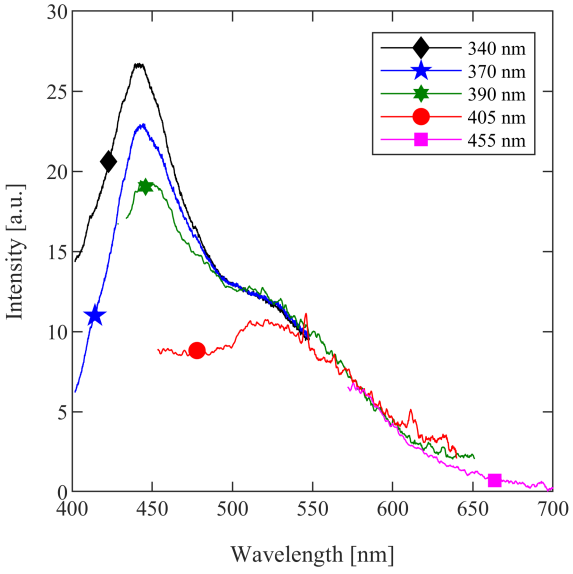

Figure 6: Fluorescence spectra of *E. coli* smears excited at 340, 370, 390, 405, and 455 nm using low-power LED modules. The spectra are scaled such that the 530-nm bands overlap.

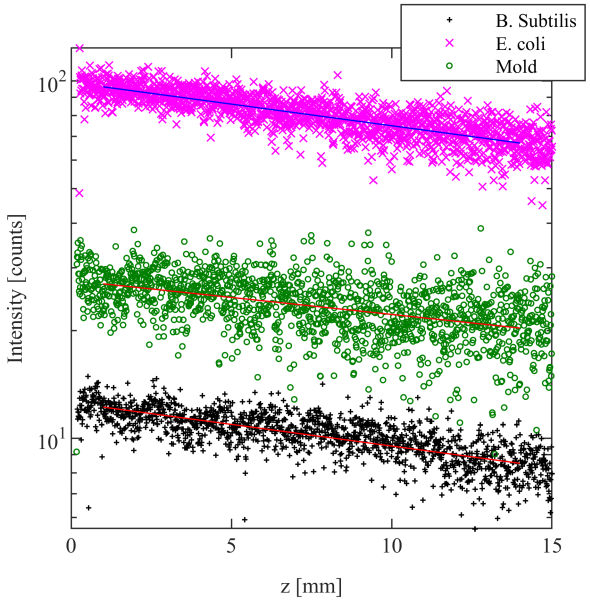

Figure 7: Average fluorescence intensity profile of aqueous suspensions measured at normal incidence, with best-fit exponential curves superimposed.

particle counting algorithm, corresponding to an extinction coefficient of 360 µm^2 per spore. Assuming a relative index of refraction of $m = 1.06$ at 632.8 nm, the effective particle diameter is 15.1 µm based on Mie's scattering solution. A nearly identical scattering cross-section value can be found from a calculation based on Gaussian path statistics [20] with a mean diameter of 15.1 µm and a standard deviation of 5 µm. Since number density is measured directly for the mold sample via particle counting, the fluorescence coefficient and fluorescence intensity per unit volume scale inversely with diameter cubed. However, since scattering is also used to measure cell concentration for the bacteria samples, this dependence is significantly reduced for *E. coli* and *B. subtilis*; for the bacteria samples, k_f and N_V scale inversely proportional to the effective diameter $\langle d_c \rangle$.

3.3. Extinction and scattering spectra

Measured extinction spectra are shown in Figure 8a. The two bacteria samples exhibit significant increases in extinction moving towards shorter wavelengths, and *E. coli* shows a factor of two increase in extinction between 400 and 300 nm. This behavior may be the result of increased absorption by proteins. The *B. subtilis* spectrum exhibits a slower increase in extinction compared to the relatively sharp cutoff observed for *E. coli* below ~400 nm. Unlike the bacteria samples, the mold extinction appears to peak near 700 nm and decreases at shorter wavelengths, which

Table 3
Measured and calculated fluorescence properties for each sample. The extinction coefficient was measured at 632.8 nm, and particle size is estimated from [13] for *E. coli* and [22] for *B. subtilis*. The mold spore size was calculated as described in the text.

Species	k_e [mm^{-1}]	n_c [mm^{-3}]	$\langle d_c \rangle$ [µm]	S [counts]	$N_{p/c}$ [-]	N_V [µm^{-3}]	k_f [mm^{-1}]
E. coli	0.030	150,000	1.2	100	1300	1.5×10^3	0.06
B. subtilis	0.045	45,000	1.7	15	5300	2.1×10^3	0.09
Green bread mold	-	13	15.1	25	1.9×10^6	1.0×10^3	0.04

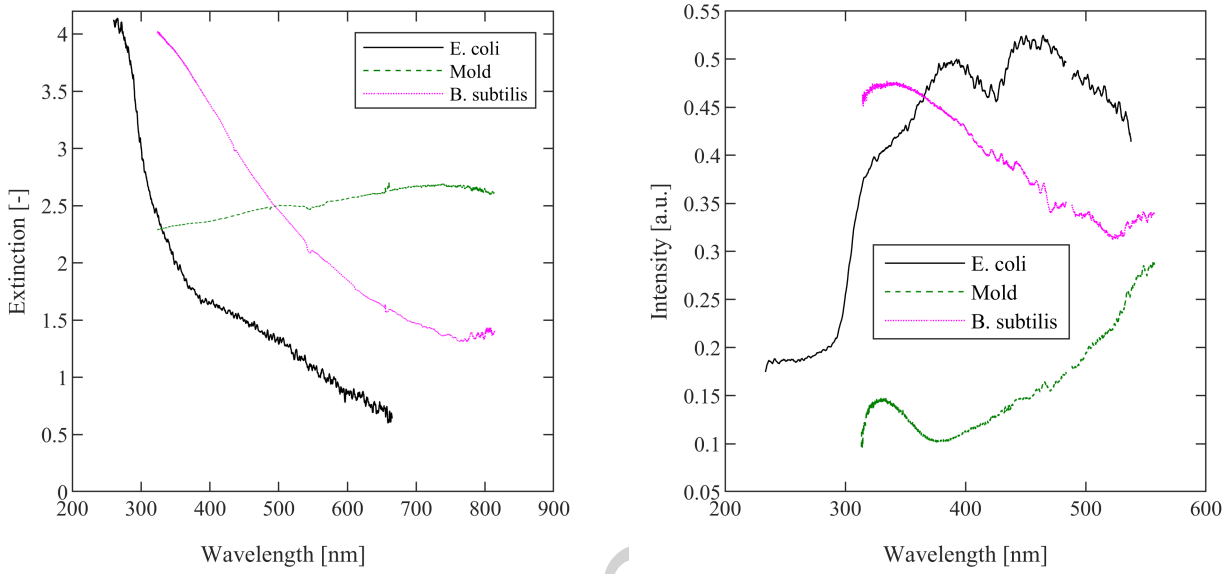

(a) Extinction (b) Elastic scattering

Figure 8: Extinction and elastic scattering spectra for *E. coli*, *B. subtilis*, and green bread smears. Small peaks due to imperfectly subtracted ambient background light are visible in the extinction spectra near 545 and 660 nm. A small region near 486 nm (the Balmer-β line) in the scattering spectra was overexposed and was masked in the plot to avoid bias.

may be related to differences in effective particle size. Note that the spectra are composite measurements that are stitched together, and may contain some additional error as a result; there are also small erroneous features near 545 nm due to imperfectly subtracted ambient background light.

The measured elastic scattering spectrum for each sample is shown in Figure 8b. The mold and *B. subtilis* spectra are consistent with the extinction measurements, suggesting that much of the observed extinction between 350 and 550 nm is likely due to scattering. The *E. coli* data at shorter wavelength is consistent with increasing absorption, *e.g.*, by proteins below 350 nm.

In contrast to the bacteria samples, the pigmentation of the mold likely influences its extinction and scattering spectra. It is not immediately clear which chemicals are responsible for the pigmentation of the samples used here. However, melanins are produced by fungi across all phyla, and fungal melanins are typically associated with dark green, brown, and black pigmentation [21]. Melanins are generally characterized by broad absorption features that cover the UV and visible spectrum, with absorption peaking at UV wavelengths, which is qualitatively consistent with the data presented here.

3.4. Fluorescence imaging of *E. coli*

A fluorescence imaging demonstration was also performed for *E. coli* at 370, 390, and 455 nm excitation. The resulting images are shown in Figure 9. From the images, the measured intensity is on the order of several thousand counts for smears on the order of 0.1 mm thick at the relatively low excitation irradiance. The near-UV LEDs are believed to primarily excite blue fluorescence from NADH, whereas the 455 nm excitation produces green fluorescence which is believed to originate from FAD. The fluorescence intensities are surprisingly similar for the different excitation strategies. Increased absorption by FAD at higher excitation wavelengths may be sufficient to make up for the decrease in NADH absorption; sensor quantum efficiency is also slightly increased at green wavelengths associated with FAD compared to the blue NADH fluorescence. Note that there is some background from the substrate that is visible on the order of several counts before applying the flatfield correction.

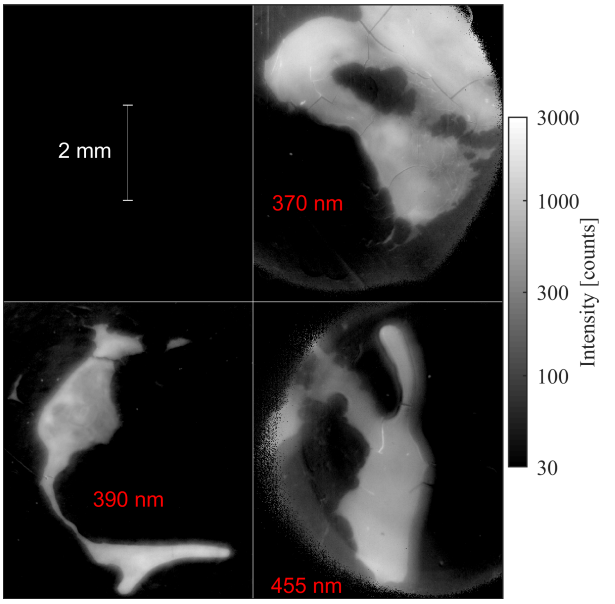

Figure 9: Averaged fluorescence images of three different *E. coli* smears with 370, 390, and 455 nm excitation.

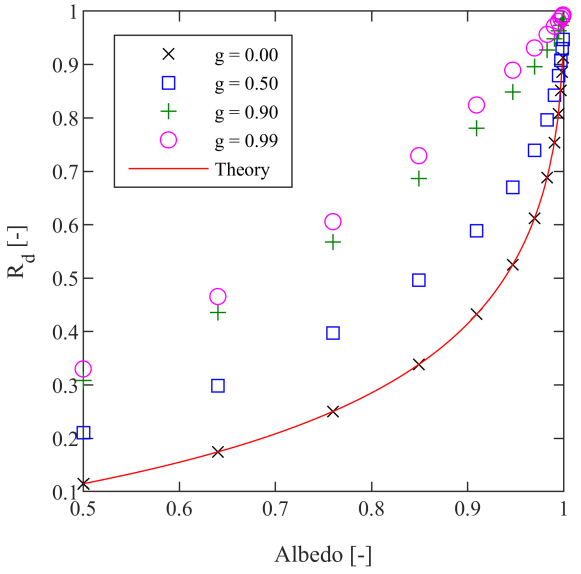

Figure 10: Calculated diffuse reflection coefficient for normally-incident pencil beam on an infinitely thick particle layer. Points are calculated from a custom Monte Carlo photon transport code with varying scattering anisotropy g and the curve is calculated from the analytical solution for isotropic scattering.

4. Analysis & Discussion

Measurements of fluorescence spectra, fluorescence intensity, scattering spectra, and extinction spectra were made for *E. coli*, *B. subtilis*, and a green bread mold fungus sample in an initial step towards characterizing a variety of microbes for potential use in imaging diagnostics. The extinction and elastic scattering spectra provide insight into bulk material effects that may limit diagnostic utility in some circumstances, such as re-absorption or radiative trapping, and may additionally have diagnostic potential. Analysis of the fluorescence spectra at different excitation wavelengths may also provide some insight into the origin of the fluorescence. Finally, fluorescence intensity measurements provide a means to estimate detection limits for different fluorescence imaging strategies. Each of these effects will be discussed in detail in this section.

4.1. Absorption characteristics

It is known that the elastic scattering or diffuse reflection spectra provide an indirect measurement of scattering and absorption properties, but the relationship between these properties is complicated. A series of calculations were performed here to gain insight into the relationship for this analysis. The total diffuse reflection coefficient from an isotropic, infinitely deep particle layer for a normally-incident beam is known to be [23]

$$R_D = 1 - H(\mu_0; \alpha)\sqrt{1-\alpha} \tag{7}$$

where α is the single-scatterer albedo and H is Chandrasekhar's H-function, which is the solution to an integral equation that also depends on α. To illustrate the solution for anisotropic scattering, a Monte Carlo photon transport simulation was run using a custom code that simulates scattering and absorption of photon packets initially normally-incident on an infinitely thick particle layer in air at several values of scattering anisotropy using the Henyey-Greenstein phase function [24]. The resulting reflection coefficients (integrated over angle) are plotted in Figure 10 for both the analytical and computational cases. The analytical calculation was implemented in Matlab based on the results of [25], and the photon transport calculation was implemented in C++ using only the C++ standard library functions.

Based on the figure, the reflection coefficient for the isotropic scattering case is not linearly dependent on albedo. In all cases, highly scattering particles ($\alpha \to 1$) have $R_D \to 1$. However, if the particles tend to absorb strongly ($\alpha < 1$) the reflection coefficient generally is smaller than the albedo ($R_D < \alpha$). Conceptually, since the particle layer is dense, a photon may be scattered multiple times before it escapes the layer and each event has an equal probability for absorption. On average, the powder layer absorbs more light per particle than a single isolated particle would absorb.

Based on the results of this analysis, it is believed that the scattering and extinction spectra presented in Section 3.3 are dominated by elastic scattering with isolated absorption features. In particular the data indicate potential absorption features at 420 nm for *E. coli*, 500 nm for *B. subtilis*, and ~380 nm for the mold sample. Increased absorption at UV wavelengths is evident as well via decreasing scattering intensity combined with increasing extinction for decreasing wavelength below ~350 nm. However, comparing the ratio of the scattering intensity to the extinction coefficient, the

Table 4
Best-fit values for NADH and FAD using 1D-CCM using spectra from [18] and [26, 27]. The assumed FQY and radiative deactivation rate A are included.

	NADH	FAD	units
T''	25,220	20,060	cm^{-1}
ν'	756	775	cm^{-1}
ν''	818	843	cm^{-1}
δ_q	3.21	2.32	-
W	500	500	cm^{-1}
μ'	3.94	4.32	Debye
μ''	3.63	2.95	Debye
Φ	0.02	0.04	-
A	48.5	17.6	MHz

additional suspected absorption features do not appear to be any stronger than the 340 and 370 nm peaks used here for fluorescence studies. For this reason, the selected 340 and 370 nm excitation wavelengths are believed to be ideal for fluorescence studies.

4.2. *E. coli* fluorescence model

To better understand diagnostic implications of the absorption and fluorescence of the microbe samples under investigation, a fluorescence model was developed for *E. coli* based on NADH and FAD photophysics and compared to the fluorescence spectra observed at different excitation wavelengths. A one-dimensional configuration coordinate model (1D-CCM) was applied to the data and to spectra that have been published previously. FAD and NADH absorption cross-section and fluorescence intensity spectra from [26, 27] and [18], respectively, were simultaneously fit to a 1D-CCM and the best-fit parameters are listed in Table 4 (see Appendix A for a discussion of the model and parameters). Note that FAD has two distinct absorption peaks likely arising from different electronic transitions; for simplicity, only the longer wavelength absorption peak near 450 nm was fit. The remaining bands used in the fits are believed to be the result of a single electronic transition (see [18] and [28]).

To adapt the individual NADH and FAD models to *E. coli*, the normal coordinate shift parameter δ_q for NADH was reduced to 2.9 to account for a blueshift caused by the chemical environment in *E. coli* that results in a fluorescence peak closer to 440 nm; a similar shift was observed in [18] for a 1:1 molar ratio of NADH with lactic dehydrogenase. Otherwise, the parameters were not changed. The relative mole fractions of the NADH and FAD components were selected to match the *E. coli* spectra at 370 nm excitation. A series of simulated fluorescence spectra were calculated using the simulated FAD and NADH fluorescence spectra, the simulated NADH absorption spectrum, and measured FAD absorption spectra from [26] assuming that the FQY of each molecule is constant at the value listed in Table 4, and the mole fraction ratio is $\chi_{\mathrm{FAD}}/\chi_{\mathrm{NADH}} = 0.35$. The simulated spectra are shown in Figure 11 normalized by their value at 550 nm.

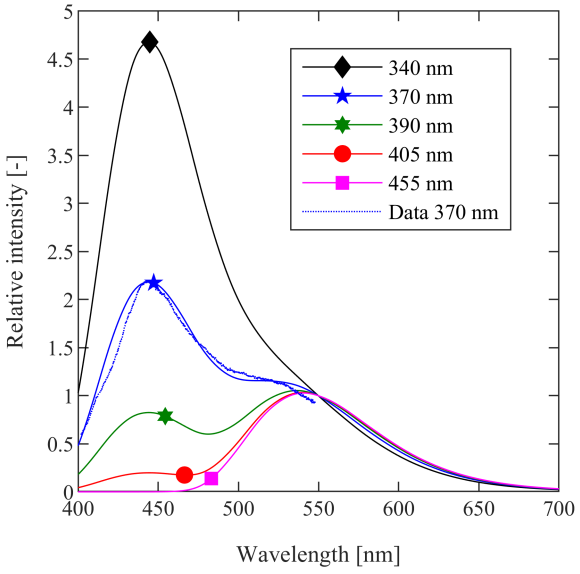

Figure 11: Simulated fluorescence spectra of *E. coli* at several excitation wavelengths, with measured spectrum at 370 nm excitation.

The simulated spectra clearly capture the features of the fluorescence emission well even without tuning the parameters to match the measurement beyond accounting for the NADH blueshift. The general trend of reduced 440 nm fluorescence peak intensity with increasing excitation wavelength is captured in the simulation, but the magnitude of the effect is overestimated. Considering the absorption spectrum of FAD peaks near 450 nm, it is very likely that the measured spectra are influenced by radiative trapping. This hypothesis is supported by the discussion from Section 4.1; since the bacteria smear is relatively thick and turbid, there is increased opportunity for absorption and subsequent emission of light. It is additionally likely that there is some change in optical properties due to the chemical environment within *E. coli* that was not considered here, and the FQY of FAD is likely not independent of excitation wavelength.

4.3. Detection limits for prototypical experiment

To illustrate the utility of microbial fluorescence imaging, performance estimates were made for a prototypical imaging experiment in which a bacterial smear of an unknown thickness is excited with a fixed irradiance of 10 mW/cm^2. It is assumed that the imaging system has a physical pixel size of 2.5 µm, and that a 50-mm focal length, $f/2.0$ lens is used for imaging. The assumed magnification is -0.5, such that the effective object plane pixel size is 5 µm, and a 1 ms exposure duration is used. The assumed optical properties are summarized in Table 5.

The detection limits for the setup are calculated to determine the smallest smear thickness or microbe volume that is capable of being imaged. The limit of detection is defined here as the point at which the imaging system signal-to-noise ratio is equal to unity. In the shot-noise limit, this is

Table 5
Assumed radiometric parameters for prototypical experiment.

Symbol	Description	Value	Units
l_{px}	Pixel size	2.5	μm
$f_{\#}$	lens f-number	2.0	-
t	Exposure duration	1	ms
M	Image magnification	-0.5	-
η_{opt}	Optical efficiency	0.9	-
η_{QE}	Sensor quantum efficiency	0.8	-
I	LED irradiance	10	$\frac{\text{mW}}{\text{cm}^2}$
λ	LED wavelength	340	nm
$\frac{\Omega}{4\pi}$	Collection fraction	5.2×10^{-3}	-

equivalent to the amount of microbes that produces enough fluorescence that one photon is detected on the sensor. The minimum smear thickness $T_{\min}$ is calculated as

$$T_{\min} = \frac{N_{\min}}{\frac{\Omega}{4\pi}\eta_{opt}\eta_{QE}\frac{It}{\hbar\omega}k_f\left(\frac{l_{px}}{M}\right)^2} \tag{8}$$

where $N_{\min}$ is the minimum number of photons needed for detection, which in this case is assumed to be one. Alternatively, the minimum microbe volume needed for detection within one pixel is given by

$$V_{\min} = T_{\min}\left(\frac{l_{px}}{M}\right)^2. \tag{9}$$

For an assumed fluorescence coefficient of 0.05 mm^{-1}, the minimum detectable smear thickness is 1.3 μm corresponding to a minimum volume of approximately 30 μm^3 per pixel or approximately 35 *E. coli* cells. Bacteria fluorescence imaging thus is capable of detecting only a handful of cells with relatively low excitation power and short exposure durations. Perhaps 50 to 100 cells may be needed to provide sufficient signal if thermal noise sources are significant. However, the most significant limitation is likely due to interfering fluorescence or reflections.

5. Conclusions

In this paper, three microbe samples (*E. coli*, *B. subtilis*, and a wild-type green bread mold fungus) were characterized spectroscopically as an initial step towards the development of fluorescence-based imaging diagnostics for the detection and identification of microbial pathogens. Fluorescence spectra, extinction spectra, and elastic scattering spectra were measured for each species, and absolute measurements of fluorescence intensity per unit volume were made at 340 nm excitation. It was found that fluorescence for each species peaks near 440 and 530 nm, which appears to correspond to NADH and FAD fluorescence, respectively, but there are modest differences in the fluorescence spectrum for each species which may provide a means of distinguishing between species in an imaging application. Further, each species emits with similar intensity per unit volume and this information was used to estimate imaging detection limits for a typical experimental setup. 340 and 370 nm are believed to be acceptable excitation wavelengths for fluorescence imaging based on modeling results and analysis of the extinction and scattering spectra. The estimated detection limit is approximately 30 μm^3 of microbes with modest excitation (10 mW/cm^2 at 340 nm) for a 1 ms exposure in the shot-noise limit. A discussion of microbial smear scattering properties and *E. coli* fluorescence was provided; based on the results and analysis, it is believed that radiative trapping likely has a significant impact on the measured spectra.

A. Spectral model

The 1D-CCM is a simplified model used to calculate absorption cross-section and fluorescence rate for a system by modeling it as a one-dimensional quantum oscillator and making use of the Franck-Condon (FC) principle. In the Condon approximation, the absorption cross-section and spontaneous radiative transition rate are independent of nuclear motion and are thus given by

$$\sigma(\omega) = \frac{4\pi^2\alpha\omega}{3e^2}|\mu'|^2\sum_{ij}\frac{e^{-\frac{G'_i}{k_BT}}}{Q'_v(T)}|\langle i|j\rangle|^2\mathcal{L}(\omega-\omega_{ij};W) \tag{10a}$$

and

$$k(\omega) = \frac{4\omega^3\alpha}{3c^2e^2}|\mu''|^2\sum_{ij}\frac{e^{-\frac{G''_j}{k_BT}}}{Q''_v(T)}|\langle i|j\rangle|^2\mathcal{L}(\omega-\omega_{ij};W) \tag{10b}$$

respectively, with transition frequency

$$\omega_{ij} = T'' + G''_j - G'_i. \tag{10c}$$

Here, ω is the radiation angular frequency, α is the fine-structure constant, e is the electron charge, c is the speed of light, $|\mu|$ is the transition dipole moment matrix element, G_l is the vibrational energy of state l, k_B is the Boltzmann constant, Q_v is the vibrational partition function, $\mathcal{L}$ is the lineshape function, and W is a smoothing parameter to account for rotational structure or other broadening that is not included explicitly (in this case a Gaussian lineshape function is used). The superscript prime ($'$) and double prime ($''$) represent the ground and excited states, respectively, and $\langle i|j\rangle$ represents the inner product of the vibrational states i and j (*i.e.*, the FC factor).

The harmonic approximation is used for simplicity. In this case, the vibrational energy for level l is $G_l = hc\nu(l+{}^1\!/_2)$ and the partition function is given by

$$Q_v(T) = \frac{e^{-\frac{hc\nu}{2k_BT}}}{1-e^{-\frac{hc\nu}{k_BT}}}. \tag{11}$$

where it is assumed that G includes the zero-point energy. The Franck-Condon matrix is calculated using the harmonic

oscillator recursion relations

$$\begin{aligned}\langle 0|j\rangle = &-\sqrt{\frac{2}{j-1}}\frac{\beta\delta_q}{1+\beta^2}\langle 0|j-1\rangle \\ &-\sqrt{\frac{j-2}{j-1}}\frac{1-\beta^2}{1+\beta^2}\langle 0|j-2\rangle\end{aligned} \tag{12a}$$

along the first row and

$$\begin{aligned}\langle i|j\rangle = &\sqrt{\frac{2}{i-1}}\frac{\beta^2\delta_q}{1+\beta^2}\langle i-1|j\rangle \\ &+\sqrt{\frac{j-1}{i-1}}\frac{2\beta}{1+\beta^2}\langle i-1|j-1\rangle \\ &+\sqrt{\frac{i-2}{i-1}}\frac{1-\beta^2}{1+\beta^2}\langle i-2|j-1\rangle\end{aligned} \tag{12b}$$

for the remaining entries where

$$\beta = \sqrt{\frac{\nu''}{\nu'}} \tag{13}$$

is the stiffness ratio and δ_q is the dimensionless normal coordinate shift between the ground and excited configurations.

Declarations

Ethical approval
Not applicable.

Competing interests
The authors have a patent pending to the Regents of the University of Michigan based in part on the results of this work.

Authors' contributions
JMH: Conceptualization, Methodology, Software, Formal Analysis, Investigation, Data Curation, Writing - Original Draft Preparation, Writing - Review & Editing, Visualization. VS: Conceptualization, Resources, Supervision, Writing - Review & Editing, Project Administration, Funding acquisition.

Funding
The authors declare that no funds, grants, or other support were received during the preparation of this manuscript.

Availability of data and materials
The datasets generated during and/or analysed during the current study are available from the corresponding author on reasonable request.

References

[1] H. Lee and Y. Yoon, "Etiological agents implicated in foodborne illness world wide," *Food science of animal resources*, vol. 41, no. 1, p. 1, 2021.

[2] M. Haque, M. Sartelli, J. McKimm, and M. A. Bakar, "Health care-associated infections–an overview," *Infection and drug resistance*, vol. 11, p. 2321, 2018.

[3] C. K. Sen, "Human wounds and its burden: an updated compendium of estimates," 2019.

[4] M. S. Ammor, "Recent advances in the use of intrinsic fluorescence for bacterial identification and characterization," *Journal of fluorescence*, vol. 17, no. 5, pp. 455–459, 2007.

[5] L. Leblanc and E. Dufour, "Monitoring the identity of bacteria using their intrinsic fluorescence," *FEMS microbiology letters*, vol. 211, no. 2, pp. 147–153, 2002.

[6] M. Sohn, D. S. Himmelsbach, F. E. Barton, and P. J. Fedorka-Cray, "Fluorescence spectroscopy for rapid detection and classification of bacterial pathogens," *Applied spectroscopy*, vol. 63, no. 11, pp. 1251–1255, 2009.

[7] F. Awad, C. Ramprasath, N. Mathivanan, P. R. Aruna, and S. Ganesan, "Steady-state and fluorescence lifetime spectroscopy for identification and classification of bacterial pathogens," *Biomedical Spectroscopy and Imaging*, vol. 3, no. 4, pp. 381–391, 2014.

[8] H. E. Giana, L. Silveira, R. A. Zângaro, and M. T. T. Pacheco, "Rapid identification of bacterial species by fluorescence spectroscopy and classification through principal components analysis," *Journal of Fluorescence*, vol. 13, no. 6, pp. 489–493, 2003.

[9] D. J. O'Connor, D. Iacopino, D. A. Healy, D. O'Sullivan, and J. R. Sodeau, "The intrinsic fluorescence spectra of selected pollen and fungal spores," *Atmospheric Environment*, vol. 45, no. 35, pp. 6451–6458, 2011.

[10] S. Saari, M. Putkiranta, and J. Keskinen, "Fluorescence spectroscopy of atmospherically relevant bacterial and fungal spores and potential interferences," *Atmospheric Environment*, vol. 71, pp. 202–209, 2013.

[11] H. Bhatta, E. M. Goldys, and R. P. Learmonth, "Use of fluorescence spectroscopy to differentiate yeast and bacterial cells," *Applied microbiology and biotechnology*, vol. 71, no. 1, pp. 121–126, 2006.

[12] J. Beal, T. Haddock-Angelli, G. Baldwin, M. Gershater, A. Dwijayanti, M. Storch, K. De Mora, M. Lizarazo, R. Rettberg, and with the iGEM Interlab Study Contributors, "Quantification of bacterial fluorescence using independent calibrants," *PloS one*, vol. 13, no. 6, p. e0199432, 2018.

[13] F. D. Bryant, B. Seiber, and P. Latimer, "Absolute optical cross sections of cells and chloroplasts," *Arch. Biochem. Biophys.*, vol. 135, pp. 97–108, 1969.

[14] G. W. Faris, R. A. Copeland, K. Mortelmans, and B. V. Bronk, "Spectrally resolved absolute fluorescence cross sections for bacillus spores," *Applied optics*, vol. 36, no. 4, pp. 958–967, 1997.

[15] N. Otsu, "A threshold selection method from gray-level histograms," *IEEE transactions on systems, man, and cybernetics*, vol. 9, no. 1, pp. 62–66, 1979.

[16] A. Bhattacharjee, R. Datta, E. Gratton, and A. I. Hochbaum, "Metabolic fingerprinting of bacteria by fluorescence lifetime imaging microscopy," *Scientific reports*, vol. 7, no. 1, pp. 1–10, 2017.

[17] I. Mihalcescu, M. V.-M. Gateau, B. Chelli, C. Pinel, and J.-L. Ravanat, "Green autofluorescence, a double edged monitoring tool for bacterial growth and activity in micro-plates," *Physical Biology*, vol. 12, no. 6, p. 066016, 2015.

[18] T. G. Scott, R. D. Spencer, N. J. Leonard, and G. Weber, "Emission properties of NADH. studies of fluorescence lifetimes and quantum efficiencies of NADH, AcPyADH, and simplified synthetic models," *J. Am. Chem. Soc*, vol. 92, no. 3, pp. 687–695, 1970.

[19] S. D. Islam, T. Susdorf, A. Penzkofer, and P. Hegemann, "Fluorescence quenching of flavin adenine dinucleotide in aqueous solution by pH dependent isomerisation and photo-induced electron transfer," *Chemical physics*, vol. 295, no. 2, pp. 137–149, 2003.

[20] M. Xu, M. Lax, and R. Alfano, "Anomalous diffraction of light with geometrical path statistics of rays and a gaussian ray approximation," *Optics letters*, vol. 28, no. 3, pp. 179–181, 2003.

[21] L. Lin and J. Xu, "Fungal pigments and their roles associated with human health," *J. Fungi*, vol. 6, no. 4, p. 280, 2020.

[22] J. Errington and L. T. van der Aart, "Microbe profile: Bacillus subtilis: model organism for cellular development, and industrial workhorse," *Microbiology*, vol. 166, no. 5, p. 425, 2020.

[23] R. Giovanelli, "Reflection by semi-infinite diffusers," *Optica Acta: International Journal of Optics*, vol. 2, no. 4, pp. 153–162, 1955.
[24] L. G. Henyey and J. L. Greenstein, "Diffuse radiation in the galaxy," *The Astrophysical Journal*, vol. 93, pp. 70–83, 1941.
[25] D. Stibbs and R. Weir, "On the H-functions for isotropic scattering," *Monthly Notices of the Royal Astronomical Society*, vol. 119, no. 5, pp. 512–525, 1959.
[26] Y.-T. Kao, C. Saxena, T.-F. He, L. Guo, L. Wang, A. Sancar, and D. Zhong, "Ultrafast dynamics of flavins in five redox states," *J. Am. Chem. Soc.*, vol. 130, no. 39, pp. 13132–13139, 2008.
[27] J. Galbán, I. Sanz-Vicente, J. Navarro, and S. De Marcos, "The intrinsic fluorescence of FAD and its application in analytical chemistry: a review," *Methods Appl. Fluoresc.*, vol. 4, no. 4, p. 042005, 2016.
[28] K. Schwinn, N. Ferré, and M. Huix-Rotllant, "UV-visible absorption spectrum of FAD and its reduced forms embedded in a cryptochrome protein," *Phys. Chem. Chem. Phys.*, vol. 22, no. 22, pp. 12447–12455, 2020.